

Neural network potential energy surface for the low temperature ring polymer molecular dynamics of the $\text{H}_2\text{CO} + \text{OH}$ reaction

Cite as: J. Chem. Phys. 154, 094305 (2021); doi: 10.1063/5.0044009

Submitted: 14 January 2021 • Accepted: 3 February 2021 •

Published Online: 2 March 2021



Pablo del Mazo-Sevillano,^{1,a)} Alfredo Aguado,¹ and Octavio Roncero^{2,b)}

AFFILIATIONS

¹Unidad Asociada UAM-CSIC, Departamento de Química Física Aplicada, Facultad de Ciencias M-14, Universidad Autónoma de Madrid, 28049 Madrid, Spain

²Instituto de Física Fundamental (IFF-CSIC), CSIC, Serrano 123, 28006 Madrid, Spain

Note: This paper is part of the JCP Special Topic on Quantum Dynamics with *Ab Initio* Potentials.

^{a)}Electronic mail: pablo.delmazo@uam.es

^{b)}Author to whom correspondence should be addressed: octavio.roncero@csic.es

ABSTRACT

A new potential energy surface (PES) and dynamical study of the reactive process of $\text{H}_2\text{CO} + \text{OH}$ toward the formation of $\text{HCO} + \text{H}_2\text{O}$ and $\text{HCOOH} + \text{H}$ are presented. In this work, a source of spurious long range interactions in symmetry adapted neural network (NN) schemes is identified, which prevents their direct application for low temperature dynamical studies. For this reason, a partition of the PES into a diabatic matrix plus a NN many-body term has been used, fitted with a novel artificial neural network scheme that prevents spurious asymptotic interactions. Quasi-classical trajectory (QCT) and ring polymer molecular dynamics (RPMD) studies have been carried on this PES to evaluate the rate constant temperature dependence for the different reactive processes, showing good agreement with the available experimental data. Of special interest is the analysis of the previously identified trapping mechanism in the RPMD study, which can be attributed to spurious resonances associated with excitations of the normal modes of the ring polymer.

Published under license by AIP Publishing. <https://doi.org/10.1063/5.0044009>

I. INTRODUCTION

The raise in the reaction rate constant at low temperatures measured in different laboratories for several organic molecules (OMs) with OH and other reactants^{1–7} opened a possible solution for the enigma of how organic molecules are generated in cold dense molecular clouds, below 10 K, in the interstellar medium. These reactions usually present reaction barriers, which make impossible the reaction at low temperatures in the gas phase. For that reason, it was assumed that these molecules were formed on cosmic ices, in cold molecular clouds at about 10 K,^{8,9} and then released to the gas phase as they evolve to hotter structures,¹⁰ such as hot cores and corinos, where they were observed.^{11–14} However, recently, several observations of OMs were made in UV-shielded cold cores at 10 K,^{15–18} which introduces the need for changing the

model. Several hypotheses were introduced, such as the possibility of chemidesorption^{19,20} and the incidence of cosmic rays²¹ and of secondary UV photons, that may induce the photodesorption. However, OMs usually present dipoles and strong binding energies, and recent experiments performed by illuminating cosmic ice precursors showed that only their photofragments are desorbed into the gas phase.^{22,23} This may suggest that the origin of OMs in the gas phase should be a combined mechanism, in which they are formed on ices, and then, their photofragments are released to the gas phase, where they suffer a reprocessing to finally end in the formation of the OM.

The reprocessing could be accelerated in the gas phase by the huge increase in the reaction rate observed in the laboratory below 100 K.^{1–7} This increase is explained by the formation of a complex between the reactants, from where they tunnel to form the

products.^{5,6} However, several transition state theory (TST) studies of the $\text{CH}_3\text{OH} + \text{OH}$ reaction^{7,24–26} did not get a so steep raise in the rate constant at low temperature, but it was much slower than the experimental results. The difference was attributed to pressure effects, which, at the microscopic level, are related to the formation of reactant-reactant or reactant-buffer gas complexes. These complexes could experience secondary collisions by adding the extra energy needed to overcome the barrier. However, due to the low densities of molecular clouds, the zero-pressure rate constant is needed in their models. It is therefore mandatory to check if TST methods can describe quantitatively the tunneling in the deep regime.

In this line, we have studied the dynamics of the reactions of OH with H_2CO and CH_3OH .^{27–30} For this purpose, full dimensional potential energy surfaces (PESs) were fitted to accurate *ab initio* calculations.^{27,28} For the $\text{H}_2\text{CO} + \text{OH}$ reaction, the QCT rate constant yields semiquantitative agreement with experimental results,⁵ while for $\text{CH}_3\text{OH} + \text{OH}$, the simulated rate constant was far too low.²⁸ To check if quantum effects could explain the difference, ring-polymer molecular dynamics (RPMD) calculations were performed on the two PESs,²⁹ finding excellent agreement in the case of methanol, but a similar semiquantitative agreement for the case of H_2CO . These good agreements could explain the experimental results and provide a good estimate of the zero-pressure rate constant at low temperature, but several problems still persist. First, below 100 K, RPMD leads to a high trapping probability, forming complexes with extremely long lifetimes (larger than several hundreds of nanoseconds) whose trajectories cannot be finished. Therefore, the reaction rate has to be evaluated by multiplying the trapping rate constant by a ratio to products that is inferred from the TST method or QCT calculations.²⁹ This could also be due to the PES, and the second problem is to improve the accuracy of the fit. The goal of this paper is to check if the high trapping rate persists, in one side, and to improve the comparison with experimental data by applying Artificial Neural Network (ANN) techniques to fit a new PES.

In this work, we shall explore different alternatives for multi-dimensional fitting with ANN techniques, including the symmetry either with permutationally invariant polynomials, PIP-NN,^{31–35} or with fundamental invariants, FI-NN.^{36,37} In addition, the channel toward $\text{HCOOH} + \text{H}$ products, absent in the previous PES,²⁷ will be included. We shall focus the attention to the problem of including long range interactions, which are crucial to simulate the dynamics at low temperature. We shall then use the new PES to perform quasi-classical trajectory (QCT) and RPMD calculations to compare with the experimental results and to analyze the formation of long-lived complexes.

This paper is organized as follows. First, a description of *ab initio* calculations is provided in Sec. II. A general description of artificial neural networks is then provided in Sec. III, focusing on the description of a new many-body scheme to accurately include the long range interactions crucial in the dynamics at low temperature in Sec. IV. With this, an overall description of the PES will be provided in Sec. V, showing the most important features. In Sec. VI, we will focus on the dynamical results of this new PES, employing both QCT and RPMD methodologies, comparing with previous theoretical and experimental results. Finally, some conclusions will be extracted together with several crucial questions to be addressed in the future.

II. AB INITIO CALCULATIONS

The reactions



are studied using the explicitly correlated coupled cluster method, RCCSD(T)-F12a/cc-pVDZ,³⁸ as implemented in the MOLPRO package.³⁹ CCSD(T) calculations are considered a benchmark, and it has recently been shown that CCSD(T)-F12 is able to reach results close to CCSD(T)/CBS, even with relatively small basis sets.^{38,40,41} The effect over reactivity from an excited electronic state has been despised. MRCI/cc-pVDZ energy calculations along the RCCSD(T)-F12 minimum energy path (MEP) show that this state becomes highly repulsive as the system approaches any of the transitions states towards $\text{HCO} + \text{H}_2\text{O}$ or $\text{HCOOH} + \text{H}$. The reader is referred to the [supplementary material](#) for a further description.

The calculated stationary points at this level of theory are rather similar to those previously reported.^{27,42–47} The energy of the transition state to form $\text{HCO} + \text{H}_2\text{O}$ is very low (of ≈ 27 meV in this work) and is the point where larger discrepancies are found among the different works, depending on the level of theory adopted. This low energy is of the order of the expected accuracy for a system with so many electrons, and the calculated height varies from positive to negative depending on the level of theory chosen. The calculations presented here are considered to be highly accurate for the available methods at the moment, keeping the calculation of single points rather affordable for the calculation of the full dimensional PES.

Reaction (1a) shows a single transition state (TS) to form $\text{HCO} + \text{H}_2\text{O}$, called TS1 (see Fig. 3), with an energy of 27.1 meV. Before this transition state, a minimum (RC1) is found at an energy of -235.8 meV. The MEP to form $\text{HCOOH} + \text{H}$, in Eq. (1b), is more complex. The system must surpass the transition state (TS2), where the OH lies over the H_2CO plane. Then, H_2CO bends, and at the same time, OH gets closer to the carbon atom. Finally, one of the H_2CO hydrogens leaves, forming HCOOH . The formation of *c*- HCOOH or *t*- HCOOH depends on whether OH rotates or not from the stationary point RC4.

For the present fit, around 180 000 *ab initio* points were added to the previously calculated ones for the PES of Ref. 27. This was needed to increase the accuracy of reaction (1a), already explored in Ref. 27, and to describe, for the first time, the channel toward $\text{HCOOH} + \text{H}$, in reaction (1b). The new points were calculated iteratively including points for the MEPs and normal modes along with those evaluated on intermediate fits. In addition, QCT and RPMD trajectories were ran on intermediate versions of the fits to populate physically accessible configurations. For each new point, the Euclidean distance³¹ to all the other points is evaluated as $d_{ab} = \sqrt{\sum_{i=1}^{15} (d_i^a - d_i^b)^2}$, where d_i^a is the *i*th interatomic distance of geometry *a*.

III. ARTIFICIAL NEURAL NETWORKS

The use of Permutationally Invariant Polynomials (PIPs) with Rydberg-type functions has widely been used to describe the PES of polyatomic systems with no many atoms.^{48,49} In these methods, few non-linear exponential parameters are used, while the linear coeffi-

coefficients of each term are fitted with a least-squares method. In order to obtain a PES that is invariant with respect to translation, rotation, and inversion, the fit of the potential is carried out as a polynomial in terms of the internuclear distances.⁵⁰ As the number of internuclear distances increases more than the number of the independent coordinate it means that, even when considering low orders of the fitted polynomial, the number of coefficients necessary to carry out the fit increases enormously with a small increase in the number of atoms in the system. This implies a limitation in the application of these methods to systems of more than 6–8 atoms. Instead, in this work, we make use of neural networks (NNs) to fit a new PES.

Feed forward neural networks⁵¹ (FFNNs) are a type of functions able to transform a vectorial input into a vectorial output, in contrast to other architectures devoted to the work on matrix⁵² or graph⁵³ representations. This kind of neural networks has been of great interest in the field of PES fitting, where a molecular representation of the system is given to the neural network, returning its potential energy. This algorithm works in a supervised way since the neural network is trained against a set of target energies, e.g., *ab initio*, usually minimizing the root mean squared error (RMSE) with the predictions.

A FFNN is characterized by the number of layers and the number of neurons at each layer, increasing the flexibility of the function as more layers and neurons are included. The computational graph for such a FFNN with two hidden layers is presented in Fig. 1. A simple rule is given to move forward in the layer structure, from the input (molecular geometry) to output (energy),

$$H_j^l = \sigma \left(\sum_i w_{ji}^l H_i^{l-1} + b_j^l \right), \quad (2)$$

where H_j^l is the j th value of the l th hidden layer, w_{ji}^l and b_j^l are the trainable weights and bias in that layer, and σ is the transfer function, which is, in general, not linear.

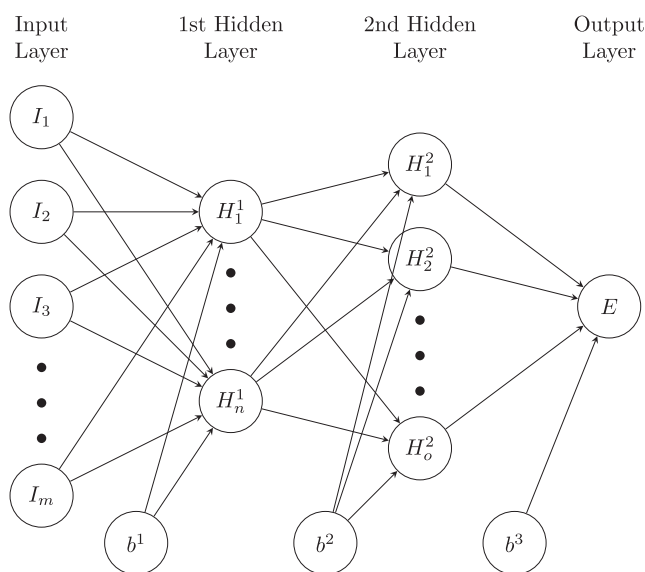


FIG. 1. Computational graph of a FFNN with two hidden layers.

Typical choices of σ are hyperbolic tangent or sigmoid functions between the hidden layers in the context of PES fitting and a linear function between the last hidden layer and the output layer to map the whole range of real numbers. In this work, we used a logistic function, $\sigma(x) = 1/(1 + \exp(-x))$, between the hidden layers. The input representation of each ANN is defined as the negative exponential of each interatomic distance. The corresponding PIP of FI polynomials is evaluated on them whenever the permutational symmetry is considered. Finally, all input values are standardized to zero mean and unit standard deviation. The PIP and FI functions used are presented in the [supplementary material](#).

The NN structure will be expressed in the usual way, $I-H_1-\dots-H_n-O$, with I and O being the number of neurons in the input and output layers and n being hidden layers, with H_i neurons in the i th hidden layer. PIP-NN and FI-NN schemes, including the permutational symmetry of identical atoms, have many properties in common, so artificial neural networks (ANNs) will be used indistinctly to refer to either PIP-NN or FI-NN in this paper.

For each permutational symmetry group, the FIs are calculated with King's algorithm⁵⁴ implemented in the computer algebra system *Singular*.⁵⁵ For many systems, these FIs have already been evaluated, and FORTRAN routines for their evaluation are provided in <https://github.com/pablomazo/FI>, expanded from the original repository <https://github.com/kjshao/FI>.

For training ANNs, we have developed NeuralPES, a Python code based on PyTorch⁵⁶ library, meant to assist at each step of the training process, beginning with data preprocessing, hyperparameter tuning, and training itself.

IV. LONG RANGE INTERACTION WITH NEURAL NETWORKS

The long range behavior of a PIP PES was analyzed in Ref. 57, concluding that certain terms of the PIP expansion lead to spurious interactions in the asymptotic region due to polynomials involving distances between unconnected fragments. This was solved by removing some of the polynomials that connect the fragments asymptotically in what is called "Purified Basis."⁵⁸ An equivalent solution was recently proposed by Li *et al.*⁵⁹ to be used in the fit of many-body (MB) terms with PIP-NN by removing those PIPs relating unconnected distances.

In this paper, we demonstrate that, on top of these terms of unconnected distances, there exists another source of spurious interactions due to the non-linearity of the transfer function in the ANN. For doing so, a simplified A_2BC system is considered, focusing on the asymptote $A_2\cdots BC$, such that there is no interaction between them. A PIP PES is defined as

$$V = \sum_i c_i \text{PIP}(i), \quad (3)$$

where c_i are the coefficients to fit and $\text{PIP}(i)$ is the i th permutational invariant polynomial. The generator of all the PIPs (G) for this particular permutational symmetry is

$$G = h_{A^1A^2}^{l_1} h_{BC}^{l_6} \left[h_{A^1B}^{l_2} \cdot h_{A^1C}^{l_3} \cdot h_{A^2B}^{l_4} \cdot h_{A^2C}^{l_5} + h_{A^2B}^{l_2} \cdot h_{A^2C}^{l_3} \cdot h_{A^1B}^{l_4} \cdot h_{A^1C}^{l_5} \right], \quad (4)$$

where $h_{ij} = f(d_{ij})$, with d_{ij} being the distance between atoms i and j , and l_{ij} is the exponent. It is common to define $h_{ij} = \exp(-\alpha d_{ij})$ such that h_{ij} tends to 0 as the distance tends to infinity. In this situation, only the PIPs where $l_2 = l_3 = l_4 = l_5 = 0$ survive in the long range,

$$G^{(\infty)} = h_{A^1A^2}^{l_1} h_{BC}^{l_6}. \quad (5)$$

Setting $\max(l_i) = 1$, the following set of PIPs is defined:

$$PIP = \{h_{A^1A^2}, h_{BC}, h_{A^1A^2} \cdot h_{BC}\}. \quad (6)$$

Therefore, the PES in the asymptote is evaluated as

$$V^{(\infty)} = c_1 \cdot h_{A^1A^2} + c_2 \cdot h_{BC} + c_3 \cdot h_{A^1A^2} \cdot h_{BC}. \quad (7)$$

Note that through the third term in the expansion, a force between A_2 and BC fragments arises, even though they were set at an infinite distance. This PIP set could be purified by just removing the third function, hence disconnecting both fragments. At this point, the asymptotic potential energy surface would depend linearly on both fragment distances, so no spurious interactions are introduced until now.

The next step is to show that even when the purified PIP set is used, PIP-NN introduces spurious interactions. In a PIP-NN, with only one hidden layer, the energy is evaluated as

$$V = \sum_j w_{Ej} H_j + b_E, \quad (8)$$

$$H_j = \sigma \left(\sum_i w_{ji} PIP(i) + b_j \right), \quad (9)$$

where w and b are the weight matrices and bias vectors, H is the hidden layer, and σ is the transfer function, which, in general, is not linear. The values of the neurons of the hidden layer evaluated on the purified PIP set become

$$H_j = \sigma(w_{j1} \cdot h_{A^1A^2} + w_{j2} \cdot h_{BC} + b_j). \quad (10)$$

Since σ is not linear, a connection between both fragments is introduced, and with that, a spurious force between them arises. $\partial V / \partial h_{A^1A^2}$ ultimately relates to the force A^1 and A^2 experience, which is given by

$$\frac{\partial V}{\partial h_{A^1A^2}} = \sum_j w_{Ej} w_{j1} \sigma'(w_{j1} \cdot h_{A^1A^2} + w_{j2} \cdot h_{BC} + b_j), \quad (11)$$

being clear that there is always a dependence with the BC fragment.

This same derivation can be developed with a set of FIs, arriving at the same conclusion. Moreover, this problem is magnified when more than one hidden layer is introduced. These spurious interactions lead to an energy transfer between the fragments, which will have a critical effect on dynamical studies, especially at low collision energies, where trajectories could even be reflected. We may then conclude at this point that the main source of spurious interactions in a PIP-NN or FI-NN is the non-linearity of the transfer function.

Although it would yield a very low fitting error, the above arguments show that it is not possible to fit the PES with one ANN since a residual interaction persists between the reactants at long distances. This causes small changes in the internal energies of each fragment,

introducing errors that strongly affect the dynamics at low energies, making inconvenient the use of PIP or FI-NN PES that expands the whole configuration space.

One possible solution is to separate the PES into two regions, short and long ranges, connected by a switching function.⁶⁰ The long range term would be a well-behaved separable function, and the short range would be an ANN PES. The main difficulty in this functional form is to tune the switching function to produce a smooth change between both regions, especially, as the dimensionality of the system increases. This can also have a huge effect when studying low energy or temperature dynamics of the system due to the possible presence of spurious matching problems.

In this work, we propose to use a partition of the potential energy as the one used in the previous PESs,^{27,28,61,62} where a diabatic matrix, V^{diab} , is used to produce a first order PES corrected with a six-body term, expressed as

$$V = E_0^{diab} + V^{6C}, \quad (12)$$

where E_0^{diab} is the lowest eigenvalue of V^{diab} . This matrix is of dimension $N \times N$, with N being the number of rearrangement channels, each of them describing reactant or product fragments and the interaction between them, including long range interactions. This matrix is analogous to those previously used^{27,28} and is described in detail in the [supplementary material](#). In the present implementation of V^{diab} , the accuracy of each fragment of the PES has been increased by replacing them by ANN fittings.

The main advantage of this form is that the diabatic matrix captures the basic features, namely, the long range interactions in each rearrangement channel and a first approximation to short range interactions, only using PESs for each of the fragments and their interactions on each rearrangement channel. This idea is based on triatomic-in-molecules (TRIMs)^{61,62} and diatomic-in-molecules (DIMs),^{63,64} which allows for an accurate description of the fragments of physical relevance and the interactions among them, both the short and long ranges.

V. POTENTIAL ENERGY SURFACE: NN SIX-BODY TERM

For the six-body term, V^{6C} , we propose to use the partition

$$V^{6C} = S \cdot V^{ANN}, \quad (13)$$

where S is the switching function, designed to be 0 as the system tends to any of the asymptotic regions, removing the spurious interaction from the V^{ANN} , the PIP-NN, or FI-NN function, trained to the difference between the *ab initio* energies and E_0^{diab} , i.e., it should tend to 0 at long distances. In this way, the switching function ensures once more that the MB term will go to 0 in the desired regions, and the fragments in the asymptotic region will not be affected by spurious interactions. On top of that, note that it is not necessary to purify the set of invariants anymore since it is the S function that removes the spurious connections.

In order to stress the importance of removing the long range spurious interaction in the ANN PES, the energy of the H_2CO and OH fragments has been followed along two QCT trajectories, both fragments being well separated so that there is no physical interaction between them. In the first trajectory, $V^{6C} = V^{ANN}$, and in the second one, $V^{6C} = S \cdot V^{ANN}$. The results are shown in [Fig. 2](#). It is clear

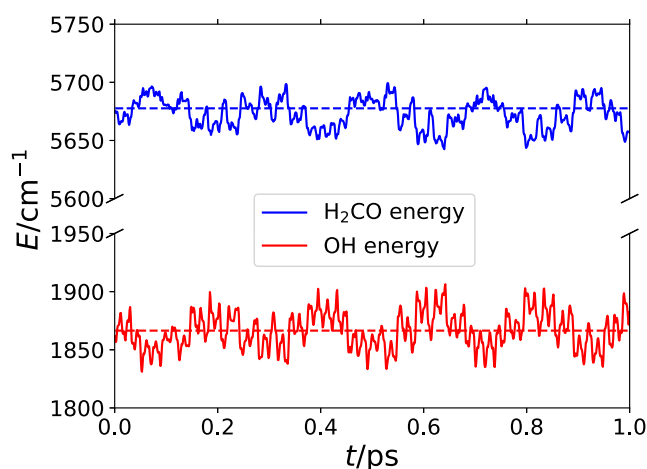


FIG. 2. Energy of H_2CO and OH fragments in two QCT trajectories with the fragments set at a large distance so that there is no physical interaction between them. Dashed lines show a trajectory in which $V^{6C} = S \cdot V^{6ANN}$, and solid lines show a trajectory where $V^{6C} = V^{6ANN}$.

that when the S function is not included to build the six-body term, both fragments experience a spurious interaction that makes their energy change along the trajectory. This transfer is of about 10 meV, comparable to the relative kinetic energy at low collisional energy. This interaction is completely removed by the switching function as it becomes evident by the constant energy of the fragments in dashed lines.

The asymptotic channels to consider in this system are $\text{H}_2\text{CO} + \text{OH}$, $\text{HCO} + \text{H}_2\text{O}$, and $\text{HCOOH} + \text{H}$. The switching function (S) is a product of hyperbolic tangents depending on the distances d_{CO} , d_{CH_1} , and d_{CH_2} , so permutational symmetry of H_2CO is preserved.

V^{6ANN} is fitted with the NeuralPES program through a FI-NN with a structure 21–80–80–1, meaning that 21 fundamental invariants are required for taking into account the permutational symmetry of the two formaldehyde hydrogen atoms. The FIs are evaluated over the negative exponential of the interatomic

TABLE I. RMSE evaluated over each energy range for the diabatic term and the full PES.

E (eV)	<Points	E_0^{diab} (meV)	V (meV)
0.0	87 356	369.38	39.18
1.0	218 522	411.41	51.98
2.0	245 978	469.64	65.79
3.0	261 437	523.92	86.45
4.0	269 743	564.00	92.05
5.0	274 326	584.60	105.60

distances. The reader is referred to the [supplementary material](#) for the hyperparameter description used here.

The RMSE of E_0^{diab} and the fitted PES are presented in Table I. The ANN V^{6C} term reduces the fitting error by almost a factor of 10 for the lower energy ranges.

In Fig. 3, the *ab initio* and the PES minimum energy paths for reactions to $\text{HCO} + \text{H}_2\text{O}$ and $\text{HCOOH} + \text{H}$ are shown. In both cases, we find very good agreement between the paths, with the only exception of a shoulder that appears in the $\text{HCOOH} + \text{H}$ product channel. This is not expected to have any effect on the dynamics since it is well below the reactants' asymptote. We find an improvement with respect to the previous PES in the description of the region of stationary point RC1, which was geometrically not well located. In addition, other local minima on the reactants' rearrangement channel, not related to the minimum energy path, have been improved, which is of importance for a reaction with such a roaming behavior.

The short range region of the PES is compared against *ab initio* results in Fig. 4. In general, the PES is very well behaved, showing perfect agreement for both attractive and repulsive regions.

Very good agreement is also found in the normal mode frequencies on the different transition states as can be checked in the table presented in the [supplementary material](#). High frequency modes have been considerably improved, in part, due to a better description of the fragment PESs. It is also found that, in general, low frequency modes present greater differences since they relate to flatter regions of the PES that can be more challenging to fit.

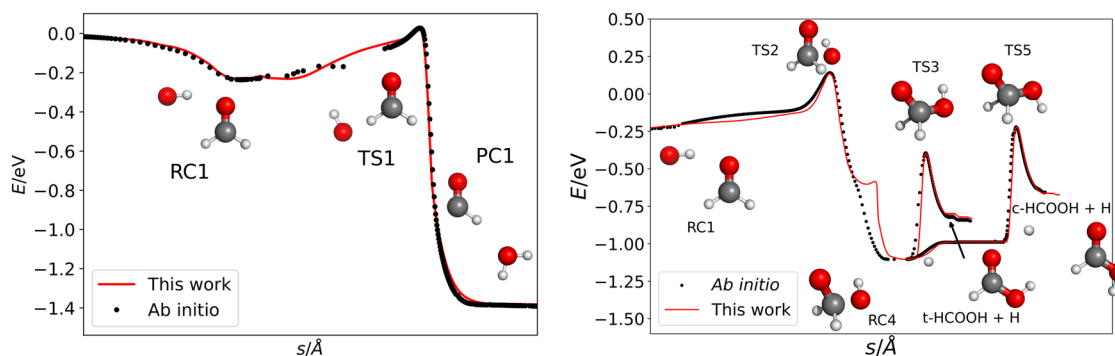


FIG. 3. Minimum energy paths for the formation of $\text{HCO} + \text{H}_2\text{O}$ (left) and $\text{HCOOH} + \text{H}$ (right), both *cis* and *trans* rotamers. The geometries of the stationary points are represented along the path.

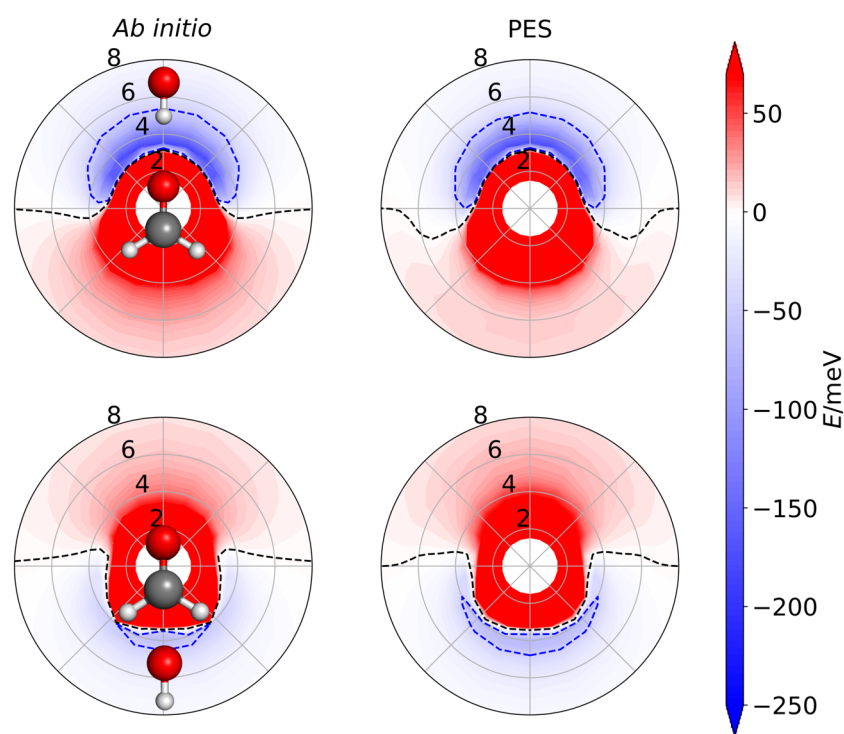


FIG. 4. Energy of the system when OH approaches H_2CO in the plane. Top (below) panels: $\text{H}(\text{O})$ of OH always faces the H_2CO molecule. Black and blue isolines represent energies of 0 meV and -50 meV, respectively. Distance is expressed in Å. The H_2CO and OH fragments are only meant to serve as a reference, and they are not at scale.

VI. DYNAMICAL RESULTS

A. QCT results

QCT calculations were carried with an extension of the miQCT code^{65,66} for N atom systems. The reaction cross section $\sigma(E)$ is calculated at fixed collision energy with the reactants in their ground vibrational and rotational states as

$$\sigma(E) = \pi b_{\max}^2 P_r(E), \quad (14)$$

where $b_{\max}(E)$ is the maximum impact parameter and $P_r(E)$ is the reaction probability at a given collision energy. The initial conditions of the internal degrees of freedom of the fragments have been calculated with the adiabatic switching method.^{67,68} The remaining initial conditions are set by random numbers according to the usual Monte Carlo method.⁶⁹ The initial maximum impact parameter is set according to the capture model for a dipole-dipole interaction^{27,70} shown in Fig. 5 along with the converged b_{\max} .

The reactive cross section for the formation of $\text{HCO} + \text{H}_2\text{O}$ is presented in Fig. 5, calculated from more than 5×10^4 trajectories at each collisional energy within $b_{\max}(E)$. The present QCT results have the same qualitative behavior as those obtained with a previous PES,^{5,27} and the reactive cross section experiences a huge increase as the collisional energy decreases below 100 meV, even at energies lower than the transition state energy barrier, at 27 meV. This increase in the reactive cross section is explained by an enormous increase in the maximum impact parameter, while the reaction probability remains constant or slightly increases.

The reaction at high relative collisional energy is characterized by a direct mechanism in which OH and H_2CO collide and either

react or fly apart. At low collisional energies, the reaction is dominated by the long range, dipole-dipole, interaction, which rotates and orients the reactants as to maximize their interaction, capturing the trajectory for high values of the impact parameter. This leads to

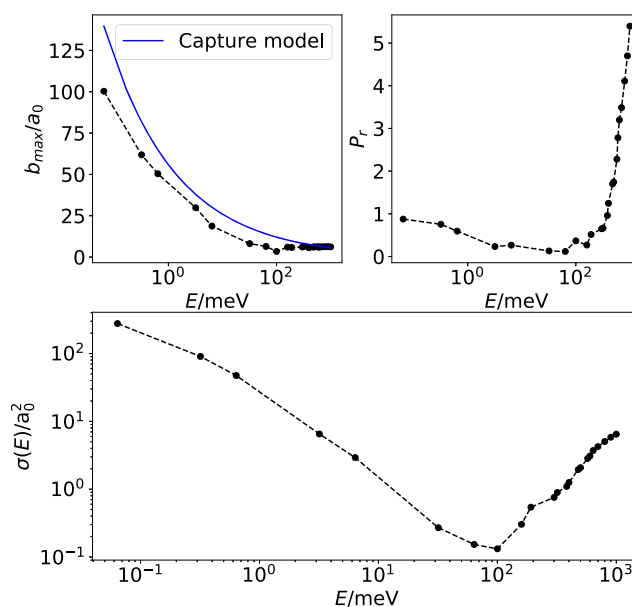


FIG. 5. QCT results at fixed collisional energy for the formation of $\text{HCO} + \text{H}_2\text{O}$. Top left panel: the maximum impact parameter. Top right panel: the reaction probability. Lower panel: the reactive cross section.

a rotational excitation of the system as the reactants become closer that traps the system for long times since it is improbable to stop the rotation turning it into translation. Direct and trapped QCT trajectories are similar to the RPMD ones, shown in Fig. 9, with the difference that trapped trajectories live much less, as will be discussed below.

The reaction probability does not go to 0 for collisional energies below the potential barrier since the zero-point energy (ZPE) is enough to overcome it. Still, there must exist couplings between the orthogonal degrees of freedom that promote the energy transfer among them. This coupling becomes favored by the roaming-like mechanism and the huge complex lifetimes experienced at low collisional energies.

The QCT reaction rate constants have been calculated at constant temperature, with the reactants in their ground vibrational states, and by considering their rotational distribution. Only the two states that correlate with the ground spin-orbit state, $\text{OH} (^2\Pi_{3/2})$, react, so the electronic partition function is

$$q_e(T) = \frac{1}{1 + \exp(-200.3/T)}, \quad (15)$$

and the reaction rate constant is evaluated as

$$k(T) = q_e(T) \sqrt{\frac{8k_B T}{\pi \mu}} \pi b_{\max}^2(T) P_r(T), \quad (16)$$

where $b_{\max}(T)$ and $P_r(T)$ are the maximum impact parameter and reaction probability at constant temperature and μ is the reduced mass of the OH, H_2CO system.

The calculated reaction rate constants are shown in Fig. 6 along with the experimental results in the temperature range from 22 K to 1200 K, together with rates calculated earlier with another PES.^{5,27}

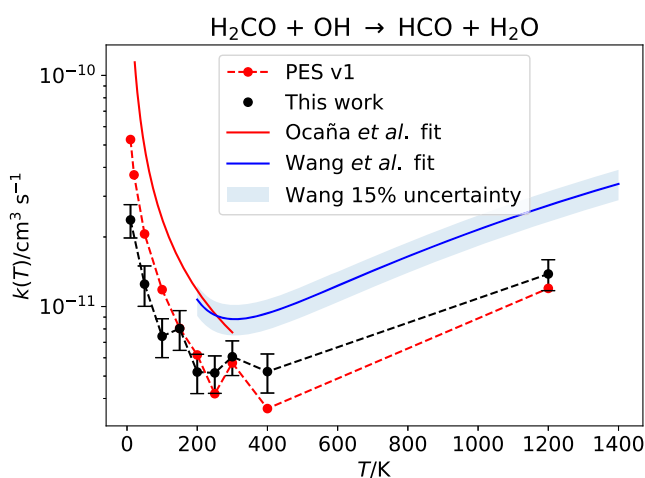


FIG. 6. QCT reaction rate constant at a constant temperature for $\text{HCO} + \text{H}_2\text{O}$ formation. Black points represent the results obtained in this work. The error bars are two times the standard error of the Monte Carlo integration.⁶⁹ Red points represent the results from our previous PES.²⁷ Solid lines represent the recommended fit from the work of Ocaña *et al.*⁵ in red and from the work of Wang *et al.*⁷¹ in blue.

The reaction rate constant behavior with temperature is basically the same for the two PESs above 100 K, but below this temperature, there is a quantitative difference between both of them, although both reproduce the increase experimentally shown. It is not surprising that the reaction rate constants calculated with the two PESs are not well reproduced at high temperatures since only the vibrational ground state of the fragments is being considered. Still, there is a factor of about 1.5 between our results and the experimental ones from the work of Wang *et al.* at 300 K. This difference increases as the temperature lowers, with respect to experimental results and also between both PESs. The discrepancies between the two PESs could be attributed to variations in the transition state region. Due to the relatively small height of the TS and the high anharmonicity of this region, tiny differences, below the fitting error, can lead to differences in dynamical behavior.

The reaction to form $\text{HCOOH} + \text{H}$ is secondary with respect to the formation of $\text{HCO} + \text{H}_2\text{O}$. In particular, Yetter *et al.*⁷² measured the kinetic rate constants for the formation of $\text{HCO} + \text{H}_2\text{O}$ to be $(7.75 \pm 1.24) \times 10^{-12} \text{ cm}^3 \text{ molecule}^{-1} \text{ s}^{-1}$, in good agreement with the present results, and $0.2_{-0.2}^{+0.8} \times 10^{-12} \text{ cm}^3 \text{ molecule}^{-1} \text{ s}^{-1}$ for $\text{HCOOH} + \text{H}$ at 300 K.

No formation of $\text{HCOOH} + \text{H}$ was observed in the RPMD trajectories described below because of the low reaction probability of this channel and the impossibility to enrich the RPMD statistics. At fixed collisional energy, the only reactivity was obtained in QCT calculations above 300 meV, which is consistent with a barrier height of 276.0 meV, including ZPE. This reaction follows a direct mechanism, where the OH approaches H_2CO in a conformation close to the one in TS2. Indeed, the maximum impact parameter for this process is about three times smaller than the one for $\text{HCO} + \text{H}_2\text{O}$ at collisional energies of 300 meV, decreasing the gap at 1 eV to 1.5 eV. As the collisional energy increases, so does the reaction probability since the system has more energy in the reaction coordinate. These results are summarized in Fig. 7.

At fixed temperature, reactivity was obtained above 900 K. It is important to remember that only reactivity from reactants in their ground vibrational states is being taken into account. Our results are in good agreement with the ones calculated by de Souza Machado *et al.*⁴⁷ with the canonical variational transition state method (CVTST) and are shown in Fig. 8.

B. RPMD results

Quantum effects, such as tunneling and zero-point energy, are important at the low temperatures of interest here. Exact quantum calculations are not feasible in this system, and one of the most successful alternative methods is Ring-Polymer Molecular Dynamics (RPMD),^{73–77} which is used in this work. RPMD is a semiclassical formalism based on Path Integral Molecular Dynamics (PIMD), which includes quantum effects such as ZPE⁷⁸ and tunneling.⁷⁹ RPMD has been successfully applied to many reactions, with barriers or deep wells.^{77,80} Here, we use the dRPMD program,⁸⁰ a direct version of the RPMD method born as an alternative to the RPMD rate code⁸¹ to deal with reactions with no barriers. dRPMD is parallelized to allow for long propagations at low temperatures, requiring many replicas or beads, N_b . The direct RPMD consists of two steps, thermalization and real-time dynamics.

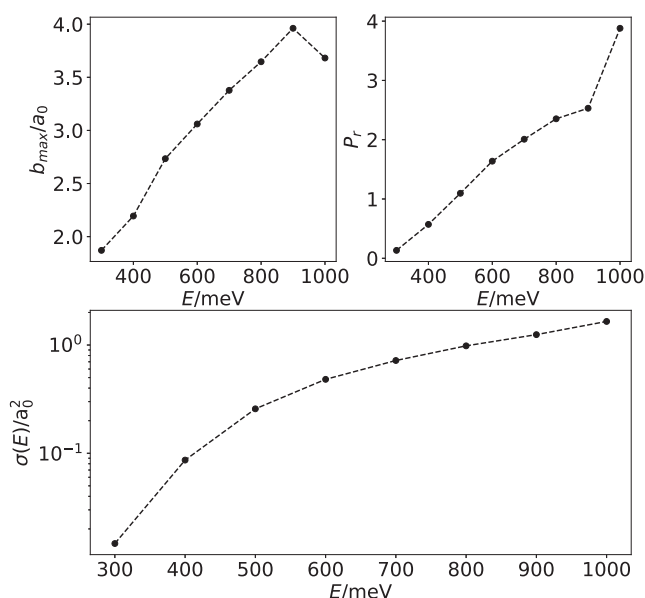


FIG. 7. QCT results at fixed collisional energy for the formation of HCOOH + H. Top left panel: the maximum impact parameter. Top right panel: the reaction probability. Lower panel: the reactive cross section.

Thermalization is a constrained PIMD simulation, which is carried out using the Andersen thermostat⁸² and freezing the distance between the two reactants at $120a_0$. This propagation is performed during 10^4 to 10^5 steps, depending on the temperature, to warrant convergence of the initial ZPE of each fragment. At the end of the thermalization, the relative position and velocities of the two reactants are reoriented, imposing a maximum initial impact parameter, similar to QCT calculations.

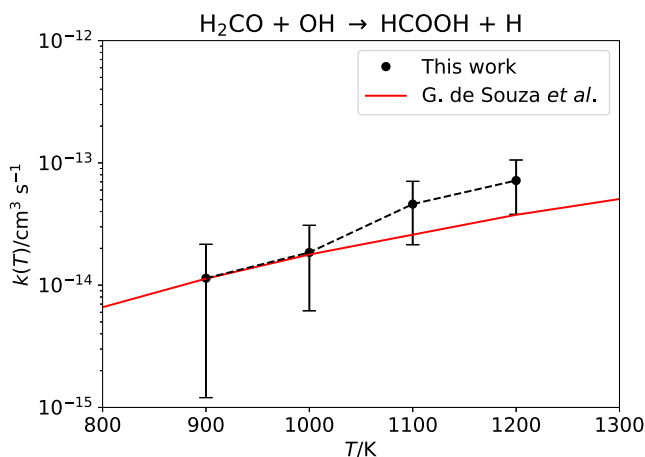


FIG. 8. QCT reaction rate constant at a constant temperature for HCOOH + H formation. The error bars are two times the standard error of the Monte Carlo integration.⁶⁹ The red line represents the results obtained by de Souza Machado et al.⁴⁷

In the second step, the constrain and the thermostat are removed, leading to the classical evolution of a system consisting of $N_{\text{atoms}} \times N_b$ particles, which are propagated using a second order symplectic operator. In previous RPMD calculations,²⁹ the symplectic propagation is separated as two steps: first, the free polymer and second, the real potential terms. The free polymer propagation was done using a Fourier transform (FT)⁸¹ and, being nearly exact, allows for a large time step. In the previous RPMD calculations,^{29,30} it was also found that for temperatures below 100 K, many trajectories were trapped in the complex well in the reactants' channel. Those trapped trajectories lived for more than 500 ns and were too long to be finished. Therefore, long-lived complexes, as compared to those obtained in QCT calculations (of several ps), could be explained by the reduction in the available reactant phase space produced in RPMD, in which ZPE is taken into account. However, it is also known that RPMD may show spurious resonances,^{83–86} which can be attributed to polymer normal mode excitations probably accessed when the frequencies of these modes are close to the frequencies associated with the “physical” system. These spurious resonances seem to be enhanced when the free ring polymer is propagated as a separate entity, and several alternatives have been proposed.^{85,86}

The choice made in this work is not to propagate the free ring polymer. Instead, we separate the ring-polymer Hamiltonian as physical kinetic energy and total potential, containing the PES among the N_{atoms} atoms and the harmonic oscillators among the beads of the same atoms. This implies to reduce the time step to approximately $\Delta t/\sqrt{N_b}$, with Δt being the time step used in the FT propagation. This reduction in the time step increases the computational time, but when using parallel computers, the present factorization reduces the communication to only neighbor processors, thus allowing for a higher speed up of parallelization.

The parameters used for the calculation of the RPMD rate constants for different temperatures are listed in Table II. At the end of each RPMD trajectory, the product channel is determined by analyzing the centroid, similarly to what is done in QCT calculations. What is different in RPMD calculations is that there is an increasing probability of trapped trajectories as temperature decreases below 300 K. Those trapped trajectories are formed following an orbit similar to the QCT orbit of Fig. 9, as those shown in previous RPMD calculations in this system:^{29,30} the long range interaction deviates the initial trajectories for rather long impact parameters, increasing the end-over-end angular momentum and the rotation of each of the two reactants. These trajectories then get trapped orbiting continuously keeping the relative orientation of the two reactants fixed, close to the geometry of the reactant well, RC1. What is different from QCT calculations is that these trapped orbits live for very long times, longer than $t_{\max} = 10$ ns in this case, when they are stopped. Thus, we give separate probabilities for direct (reactive RPMD trajectories) and trapped trajectories in Table II. The rates for direct reaction and trapping processes are then evaluated through Eq. (16), as listed in Table II.

The trapping mechanism becomes significant at temperatures below 200 K, where trajectories finished after 10 ns without dissociation or reaction. These results perfectly mimic the ones from our previous work,²⁹ as shown in Fig. 10. As compared to our previous PES, the trapping mechanism begins at temperatures slightly higher, around 300 K. With respect to the direct mechanism rate, the

TABLE II. Parameters of the direct RPMD and rate constants.

T (K)	N_b	N_{total}	t_{max} (ns)	b_{max}^{dir}/a_0	b_{max}^{trap}/a_0	P_{dir}	P_{trap}	k_{dir} (cm ³ s ⁻¹)	k_{trap} (cm ³ s ⁻¹)
1200	144	10 000	1.0	8.44	0.00	0.025	0.00	1.31×10^{-11}	0.00
1000	48	2454	0.1	5.82	0.00	0.048	0.00	1.10×10^{-11}	0.00
800	144	3749	0.1	7.93	0.00	0.019	0.00	7.21×10^{-12}	0.00
600	144	4649	0.1	6.76	0.00	0.026	0.00	6.67×10^{-12}	0.00
400	96	6695	0.1	6.93	0.00	0.016	0.00	3.82×10^{-12}	0.00
300	240	30 000	1.0	11.93	7.86	0.003	2.59×10^{-4}	2.18×10^{-12}	7.11×10^{-14}
200	384	20 000	1.0	11.78	13.82	0.005	2.01×10^{-3}	2.58×10^{-12}	1.54×10^{-12}
100	768	1000	1.0	12.95	16.60	0.003	1.94×10^{-1}	1.92×10^{-12}	1.83×10^{-10}
50	1536	400	1.0	13.39	18.96	0.015	5.89×10^{-1}	7.15×10^{-12}	5.72×10^{-10}
20	3072	143	1.0	14.53	21.43	0.048	6.40×10^{-1}	1.75×10^{-11}	5.11×10^{-10}

difference found in the QCT study seems to magnify. On top of what is already given in Sec. VI A, it is worth noting that some of the errors may emerge from a poorer statistic due to the huge computational cost of RPMD trajectories at these low temperatures. A typical trapped RPMD trajectory is shown in the left panels of Fig. 9, compared with direct and complex-forming QCT

trajectories shown in the right panels of Fig. 9. The first difference in both trajectories is that RPMD trajectory keeps trapped for much longer times than the QCT trajectory, which actually manages to break the reactive complex in the propagation time. Once the two reactants collide, ϕ_R oscillates quasiperiodically in both cases, but the angle θ_{R-OH} vector remains almost constant. This behavior is

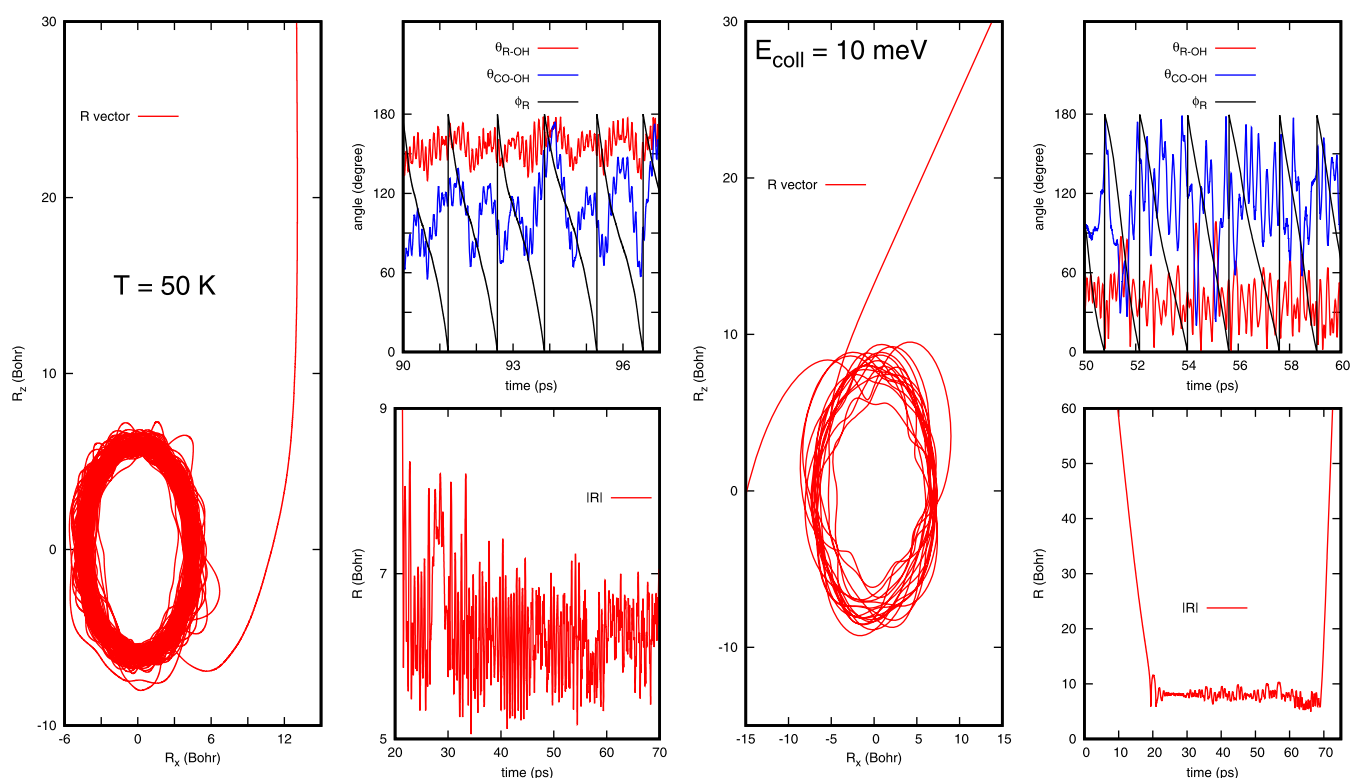


FIG. 9. Typical trapped RPMD trajectory (left three panels) obtained at 50 K. Right panels show a typical QCT trajectory for a high (red) initial impact parameter, at a fixed collisional energy of 0.1 meV. In each case, the left panel shows the components R_x and R_z of the vector, \mathbf{R} , connecting the centers of mass of the reactants along the trajectory. The right bottom panels show the modulus of \mathbf{R} as a function of time. The right top panels show the evolution of the angles: between \mathbf{R} and the OH internuclear vector, θ_{R-OH} , between the CO and OH internuclear vectors, θ_{CO-OH} , and the azimuthal angle associated with \mathbf{R} , ϕ .

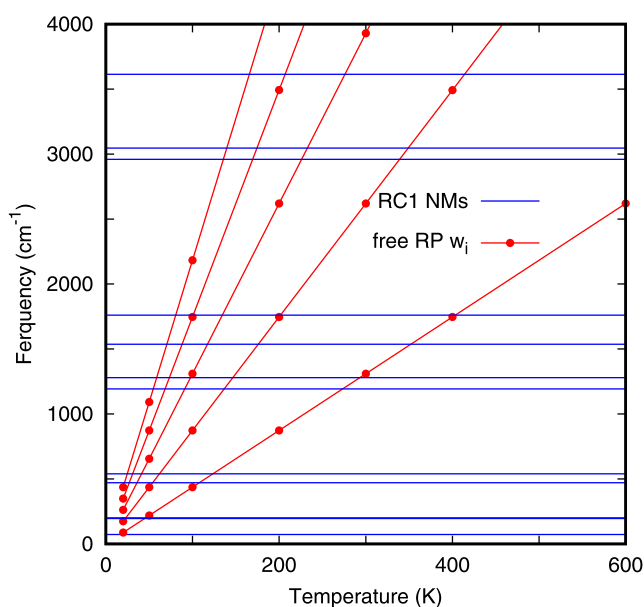


FIG. 10. Reaction and trapping rates for the present PES, compared with the ones from out previous fit.

endorsed by the θ_{CO-OH} angle, and the only appreciable difference is that QCT amplitudes have larger variations.

With respect to our previous work,²⁹ not only the partition of the RP Hamiltonian has been varied but also the time step, Δt , has been reduced by a factor of 10 and the number of beads used in the low temperature calculations has been considerably increased, in order to check whether or not long-lived complex lifetimes are artificially due to poor convergence. The computational cost of this PES has been considerably reduced, which has enabled to perform this kind of study. However, the formation of extremely long trapped trajectories persists here, as shown in Fig. 10. Therefore, we discard the possibility of this results being a lack of convergence of the calculations. Similar behavior was also found for other reactions at low temperature, $OH + CH_3OH$,²⁹ $D + H_3^+$,⁸⁷ and $H_2 + H_3^+$.⁸⁰ We therefore conclude that the trapping is a rather general outcome of RPMD calculations at low temperature.

An increase in complex lifetimes when including quantum effects is expected and can be explained according to the Rice-Ramsperger-Kassel-Marcus (RRKM) statistical theory^{88,89} by the descent of accessible dissociative states in the RPMD calculations with respect to the QCT ones because ZPE is included. However, the impossibility to end the trapped trajectories, dominant at low temperatures, seems to indicate that the RPMD method fails to reproduce the real lifetime of the reaction complexes. This is attributed to the appearance of spurious resonances as those reported previously,^{83,84} which appear when the frequency of the complexes is of the order of those of the ring-polymer modes. The normal modes of the free ring polymers⁹⁰ are given by $\omega_k = 2N_b k_B T / \hbar \sin(|k|\pi/N_b)$, with k_B being the Boltzmann constant and $-N_b/2 \leq k \leq N_b/2$. The lowest frequency mode, $k = 1$, for large N_b can be approximated by $\omega_1 \approx 2\pi T k_B / \hbar$, and when this quantity is of

the order of the lower frequency of the reaction complex, the energy flow between the “physical” and “free ring-polymer” modes may be enhanced, giving rise to spurious resonances, in which the energy is stored in the free ring-polymer normal modes. The lower ω_i are plotted as a function of temperature and compared with the physical frequencies of the H_2CO -complex in Fig. 11. Clearly, at ≈ 100 K, the first RP normal mode is of the order of the lower RC1 normal modes. As the temperature decreases, there are ring-polymer modes in near resonance with several physical modes of the RC1 complex, favoring the energy transfer. Since the density of the RP modes is large, the energy is stored there for very long times, giving rise to artificial trapping or spurious resonances.

Several solutions have been proposed to solve the problem of spurious resonances in RPMD calculations of spectra.^{83,84} Among them, the inclusion of a thermostat to the internal modes of the ring polymer during the dynamics⁸⁴ is considered here that may affect the reaction dynamics because the extra energy of the beads is expected to flow to the physical bonds, producing their fragmentation. A detailed analysis needs to be done before applying it to reactive collisions at low temperatures. Instead, in order to get the total reaction rate constant, we have to look for an alternative method to consider the fragmentation ratio of the trapped trajectories: back to reactants (redissociation) and tunneling through reaction barriers to products (tunnel). Under this assumption, the total reaction rate becomes

$$k(T) = k_{dir}(T) + k_{CF}(T), \quad (17)$$

$$k_{CF}(T) = k_{trap}(T) \frac{k_{tunnel}(T)}{k_{tunnel}(T) + k_{rediss}(T)}, \quad (18)$$

where k_{dir} is the rate constant for the direct mechanism and k_{CF} is the product of the trapping rate constant and the ratio of tunneling trajectories toward products. This approach was suggested before,^{29,30} and the ratios were obtained either from TST or QCT methods. Here, we adopted the QCT reaction probability as

$$\frac{k_{tunnel}(T)}{k_{tunnel}(T) + k_{rediss}(T)} \approx P_r^{QCT}(T), \quad (19)$$

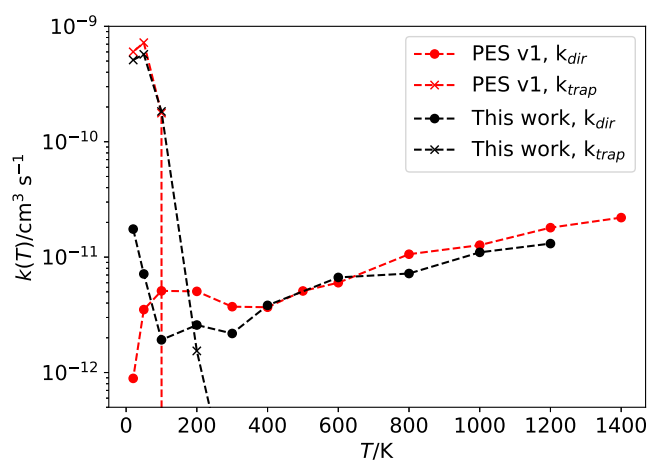


FIG. 11. RC1 complex normal mode frequencies (blue) and first five ω_i free ring-polymer frequencies vs temperature.

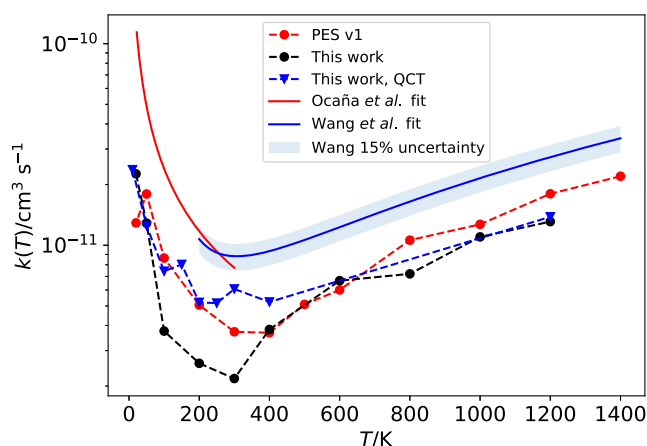


FIG. 12. RPMD reactive rate constant for $\text{HCO} + \text{H}_2\text{O}$ formation. Black points represent the RPMD results obtained in this work. Blue triangles represent the QCT results obtained in this work. Red points represent the results from our previous PES.²⁷ Solid lines show the recommended fit from the work of Ocaña *et al.*⁵ in red and from the work of Wang *et al.*⁷¹ in blue.

that is, $\sim 1\%$ for collision energies below 1 meV. This classical estimate is justified by the small height of the TS, which can even be reduced due to anharmonic effects. The resulting RPMD reaction rate constants are shown in Fig. 12 compared with previous results. The behavior of both results is similar and always below the experimental values.

Black points and blue triangles represent the RPMD and QCT results obtained in this work, respectively. Red points represent the RPMD results from our previous PES.²⁷ Solid lines show the recommended fit from the work of Ocaña *et al.*⁵ in red and from the work of Wang *et al.*⁷¹ in blue.

The difference between simulated and experimental rate constants for $T > 400$ K is attributed to the appearance of other mechanisms, such as non-adiabatic contributions of the excited electronic state and/or a lack of accuracy to describe other channels such as the $\text{H} + \text{HCOOH}$ product channel. In this work, we focus on the lower temperature behavior. Here, the problem is to determine the tunneling/redissociation fraction of the trapped RPMD trajectories. Such a study is fundamental for astrochemistry since it is necessary to use the pure zero-pressure rate constant for the formation of the OM in cold environments.

In addition, it is important to determine the lifetime of the reaction complexes to establish the role of complexes (or pressure) in the measured rate constants in CRESU experiments. Work in this direction is now on the way, following the preliminary arguments already published.³⁰

VII. CONCLUSIONS

In this work, a new full dimensional potential energy surface has been developed for the title reaction based on artificial neural networks. The long range behavior of the ANN has been analyzed in detail. A source of spurious interactions has been identified due to the non-linearity of the transfer function in the ANN, which mixes

the internal degrees of freedom of each of the polyatomic fragments. These spurious interactions change the energy of the fragments at very long distances, introducing artifacts in the dynamics at low energies, thus becoming inappropriate to study reactivity at low temperatures.

To solve this problem, a new factorization of the potential is proposed consisting of two terms, a diabatic matrix and a full dimensional term, V^{MB} , expanded using neural networks. In the diabatic matrix, the diagonal elements describe each rearrangement channel, including the potential of each independent fragment plus their interaction among them, with the long range interaction properly set. Thus, V^{MB} fits the difference and tends to 0 at intermediate distance. This term is further multiplied by a switching function to fully remove the spurious long range interaction introduced by the artificial neural network function. The present potential is more accurate than the previous one²⁷ and also incorporates the channel toward the $\text{HCOOH} + \text{H}$ product channel.

This PES has been used to calculate the reaction rate constants using QCT and RPMD methods. It is found that the $\text{HCOOH} + \text{H}$ products present a near negligible contribution at the energy range considered. The $\text{HCO} + \text{H}_2\text{O}$ reaction rate constant presents a non-Arrhenius V shape as a function of temperature, dominated by a direct mechanism at high temperatures and a complex forming at low energies, as was also found in the previous PES²⁹ and in qualitative agreement with the available experimental data.⁵

Despite the changes done in the calculations, the RPMD results show an increasing trapping probability as the temperature decreases, as reported before.²⁹ This is attributed to the presence of spurious resonances occurring when the free ring-polymer normal mode frequencies enter in near resonance with the low intermolecular normal mode frequencies. It is crucial to determine the lifetime of these complexes and the fragmentation ratio in order to properly determine the zero-pressure reaction rate constant, needed in astrophysical models, and to determine the role of complexes in the measurements made in Laval expansions. Some work in these directions is nowadays underway.

SUPPLEMENTARY MATERIAL

See the [supplementary material](#) for the multi-reference calculations of ground and first electronic states along with the MEP, the diabatic matrix, V^{diab} construction, the hyper-parameters used in the NN fits, and the normal mode frequencies in the transition states. A FORTRAN 90 implementation of this potential energy surface is also provided.

ACKNOWLEDGMENTS

This research was funded by the MICIU (Spain) under Grant No. FIS2017-83473-C2. We also acknowledge computing time at Finisterre (CESGA) and MareNostrum (BSC) under the RES computational grant (Nos. ACCT-2019-3-0004 and AECT-2020-1-0003).

DATA AVAILABILITY

The data that support the findings of this study are available from the corresponding author upon reasonable request.

REFERENCES

- ¹R. J. Shannon, M. A. Blitz, A. Goddard, and D. E. Heard, "Accelerated chemistry in the reaction between the hydroxyl radical and methanol at interstellar temperatures facilitated tunnelling," *Nat. Chem.* **5**, 745 (2013).
- ²J. C. Gómez Martín, R. L. Caravan, M. A. Blitz, D. E. Heard, and J. M. C. Plane, "Low temperature kinetics of the $\text{CH}_3\text{OH} + \text{OH}$ reaction," *J. Phys. Chem. A* **118**, 2693 (2014).
- ³R. L. Caravan, R. J. Shannon, T. Lewis, M. A. Blitz, and D. E. Heard, "Measurements of rate coefficients for reactions of OH with ethanol and propan-2-ol at very low temperatures," *J. Phys. Chem. A* **119**, 7130 (2015).
- ⁴M. Antiñolo, M. Agúndez, E. Jiménez, B. Ballesteros, A. Canosa, G. E. Dib, J. Albaladejo, and J. Cernicharo, "Reactivity of OH and CH_3OH between 22 and 64 K: Modeling the gas phase production of CH_3O in Barnard 1b," *Astrophys. J.* **823**, 25 (2016).
- ⁵A. J. Ocaña, E. Jiménez, B. Ballesteros, A. Canosa, M. Antiñolo, J. Albaladejo, M. Agúndez, J. Cernicharo, A. Zanchet, P. del Mazo, O. Roncero, and A. Aguado, "Is the gas phase $\text{OH} + \text{H}_2\text{CO}$ reaction a source of HCO in interstellar cold dark clouds? A kinetic, dynamics and modelling study," *Astrophys. J.* **850**, 28 (2017).
- ⁶D. E. Heard, "Rapid acceleration of hydrogen atom abstraction reactions of OH at very low temperatures through weakly bound complexes and tunneling," *Acc. Chem. Res.* **51**, 2620–2627 (2018).
- ⁷A. J. Ocaña, S. Blázquez, A. Potapov, B. Ballesteros, A. Canosa, M. Antiñolo, L. Vereecken, J. Albaladejo, and E. Jiménez, "Gas-phase reactivity of CH_3OH toward OH at interstellar temperatures (11.7–177.5 K): Experimental and theoretical study," *Phys. Chem. Chem. Phys.* **21**, 6942 (2019).
- ⁸R. L. Hudson and M. H. Moore, "Laboratory studies of the formation of methanol and other organic molecules by water + carbon monoxide radiolysis: Relevance to comets, icy satellites, and interstellar ices," *Icarus* **140**, 451 (1999).
- ⁹N. Watanabe, O. Mouri, A. Nagaoka, T. Chigai, A. Kouchi, and V. Pirronello, "Laboratory simulation of competition between hydrogenation and photolysis in the chemical evolution of H_2O -CO ice mixtures," *Astrophys. J.* **668**, 1001 (2007).
- ¹⁰R. T. Garrod and E. Herbst, "Formation of methyl formate and other organic species in the warm-up phase of hot molecular cores," *Astron. Astrophys.* **457**, 927–936 (2006).
- ¹¹L. E. Snyder, D. Buhl, B. Zuckerman, and P. Palmer, "Microwave detection of interstellar formaldehyde," *Phys. Rev. Lett.* **22**, 679 (1969).
- ¹²J. A. Ball, C. A. Gottlieb, A. E. Lilley, and H. E. Radford, "Detection of methyl alcohol in Sagittarius," *Astrophys. J.* **162**, L203 (1970).
- ¹³C. A. Gottlieb, P. Palmer, L. J. Rickard, and B. Zuckerman, "Studies of interstellar formamide," *Astrophys. J.* **182**, 699–710 (1973).
- ¹⁴P. D. Godfrey, R. D. Brown, B. J. Robinson, and M. W. Sinclair, "Discovery of interstellar methanimine (formaldimine)," *Astrophys. Lett.* **13**, 119 (1973).
- ¹⁵A. J. Remijan, J. M. Hollis, L. E. Snyder, P. R. Jewell, and F. J. Lovas, "Methyltriacetylene ($\text{CH}_3\text{C}_6\text{H}$) toward TMC-1: The largest detected symmetric top," *Astrophys. Lett.* **643**, L37–L40 (2006).
- ¹⁶A. Bacmann, V. Taquet, A. Faure, C. Kahane, and C. Ceccarelli, "Detection of complex organic molecules in a prestellar core: A new challenge for astrochemical models," *Astron. Astrophys.* **541**, L12 (2012).
- ¹⁷J. Cernicharo, N. Marcelino, E. Roueff, M. Gerin, A. Jiménez-Escobar, and G. M. Muñoz Caro, "Discovery of the methoxy radical, CH_3O , toward B1: Dust grain and gas-phase chemistry in cold dark clouds," *Astrophys. J. Lett.* **759**, L43 (2012).
- ¹⁸C. Vastel, C. Ceccarelli, B. Lefloch, and R. Bachiller, "The origin of complex organic molecules in prestellar cores," *Astrophys. J. Lett.* **795**, L2 (2014).
- ¹⁹S. Cazaux, M. Minissale, F. Dulieu, and S. Hocuk, "Dust as interstellar catalyst. II. How chemical desorption impacts the gas," *Astron. Astrophys.* **585**, A55 (2016).
- ²⁰Y. Oba, T. Tomaru, T. Lamberts, A. Kouchi, and N. Watanabe, "An infrared measurement of chemical desorption from interstellar ice analogues," *Nat. Astron.* **2**, 228–232 (2018).
- ²¹M. Mainitz, C. Anders, and H. M. Urbassek, "Irradiation of astrophysical ice grains by cosmic-ray ions: A REAX simulation study," *Astron. Astrophys.* **592**, A35 (2016).
- ²²G. A. Cruz-Díaz, R. Martín-Doménech, G. M. Muñoz-Caro, and Y.-J. Chen, "The negligible photodesorption of methanol ice and the active photon-induced desorption of its irradiation products," *Astron. Astrophys.* **592**, A68 (2016).
- ²³M. Bertin, C. Romanzin, M. Doronin, L. Philippe, P. Jeseck, N. Ligterink, H. Linart, X. Michaut, and J.-H. Fillion, "UV photodesorption of methanol in pure and CO-rich ices: Desorption rates of the intact molecule and of the photofragments," *Astrophys. J. Lett.* **817**, L12 (2016).
- ²⁴W. Siebrand, Z. Smedarchina, E. Martínez-Núñez, and A. Fernández-Ramos, "Methanol dimer formation drastically enhances hydrogen abstraction from methanol by OH at low temperature," *Phys. Chem. Chem. Phys.* **18**, 22712 (2016).
- ²⁵L. G. Gao, J. Zheng, A. Fernández-Ramos, D. G. Truhlar, and X. Xu, "Kinetics of the methanol reaction with OH at interstellar, atmospheric, and combustion temperatures," *J. Am. Chem. Soc.* **140**, 2906–2918 (2018).
- ²⁶T. L. Nguyen, B. Ruscic, and J. F. Stanton, "A master equation simulation for the $\text{OH} + \text{CH}_3\text{OH}$ reaction," *J. Chem. Phys.* **150**, 084105 (2019).
- ²⁷A. Zanchet, P. del Mazo, A. Aguado, O. Roncero, E. Jiménez, A. Canosa, M. Agúndez, and J. Cernicharo, "Full dimensional potential energy surface and low temperature dynamics of the $\text{H}_2\text{CO} + \text{OH} \rightarrow \text{HCO} + \text{H}_2\text{O}$ reaction," *Phys. Chem. Chem. Phys.* **20**, 5415 (2018).
- ²⁸O. Roncero, A. Zanchet, and A. Aguado, "Low temperature reaction dynamics for $\text{CH}_3\text{OH} + \text{OH}$ collisions on a new full dimensional potential energy surface," *Phys. Chem. Chem. Phys.* **20**, 25951 (2018).
- ²⁹P. del Mazo-Sevillano, A. Aguado, E. Jiménez, Y. V. Suleimanov, and O. Roncero, "Quantum roaming in the complex forming mechanism of the reactions of OH with formaldehyde and methanol at low temperature and zero pressure: A ring polymer molecular dynamics approach," *J. Phys. Chem. Lett.* **10**, 1900 (2019).
- ³⁰F. Naumkin, P. del Mazo-Sevillano, A. Aguado, Y. V. Suleimanov, and O. Roncero, "Zero- and high-pressure mechanisms in the complex forming reactions of OH with methanol and formaldehyde at low temperatures," *ACS Earth Space Chem.* **3**, 1158 (2019).
- ³¹B. Jiang and H. Guo, "Permutation invariant polynomial neural network approach to fitting potential energy surfaces," *J. Chem. Phys.* **139**, 054112 (2013).
- ³²J. Li, B. Jiang, and H. Guo, "Permutation invariant polynomial neural network approach to fitting potential energy surfaces. II. Four-atom systems," *J. Chem. Phys.* **139**, 204103 (2013).
- ³³J. Li and H. Guo, "Communication: An accurate full 15 dimensional permutationally invariant potential energy surface for the $\text{OH} + \text{CH}_4 \rightarrow \text{H}_2\text{O} + \text{CH}_3$ reaction," *J. Chem. Phys.* **143**, 221103 (2015).
- ³⁴B. Jiang, J. Li, and H. Guo, "Potential energy surfaces from high fidelity fitting of *ab initio* points: The permutation invariant polynomial—Neural network approach," *Int. Rev. Phys. Chem.* **35**, 479–506 (2016).
- ³⁵B. Jiang, J. Li, and H. Guo, "High-fidelity potential energy surfaces for gas-phase and gas-surface scattering processes from machine learning," *J. Phys. Chem. Lett.* **11**, 5120–5131 (2020).
- ³⁶K. Shao, J. Chen, Z. Zhao, and D. H. Zhang, "Communication: Fitting potential energy surfaces with fundamental invariant neural network," *J. Chem. Phys.* **145**, 071101 (2016).
- ³⁷X. Lu, K. Shao, B. Fu, X. Wang, and D. H. Zhang, "An accurate full-dimensional potential energy surface and quasiclassical trajectory dynamics of the $\text{H} + \text{H}_2\text{O}_2$ two-channel reaction," *Phys. Chem. Chem. Phys.* **20**, 23095–23105 (2018).
- ³⁸G. Knizia, T. B. Adler, and H.-J. Werner, "Simplified CCSD(T)-F12 methods: Theory and benchmarks," *J. Chem. Phys.* **130**, 054104 (2009).
- ³⁹H.-J. Werner, P. J. Knowles, G. Knizia, F. R. Manby, M. Schütz *et al.*, Molpro, version 2015.1, a package of *ab initio* programs, 2015.
- ⁴⁰T. B. Adler, G. Knizia, and H.-J. Werner, "A simple and efficient CCSD(T)-F12 approximation," *J. Chem. Phys.* **127**, 221106 (2007).
- ⁴¹Y. Ajili, K. Hammami, N. E. Jaidane, M. Lanza, Y. N. Kalugina, F. Lique, and M. Hochlaf, "On the accuracy of explicitly correlated methods to generate potential energy surfaces for scattering calculations and clustering: Application to the HCl -He complex," *Phys. Chem. Chem. Phys.* **15**, 10062–10070 (2013).
- ⁴²J. S. Francisco, "An examination of substituent effects on the reaction of OH radicals with HXCO (where $\text{X}=\text{H}$, F , and Cl)," *J. Chem. Phys.* **96**, 7597–7602 (1992).
- ⁴³J. R. Alvarez-Idaboy, N. Mora-Díez, R. J. Boyd, and A. Vivier-Bunge, "On the importance of prereactive complexes in molecule-radical reactions: Hydrogen abstraction from aldehydes by OH," *J. Am. Chem. Soc.* **123**, 2018–2024 (2001).

- ⁴⁴B. D'Anna, V. Bakken, J. Are Beukes, C. J. Nielsen, K. Brudnik, and J. T. Jodkowski, "Experimental and theoretical studies of gas phase NO_3 and OH radical reactions with formaldehyde, acetaldehyde and their isotopomers," *Phys. Chem. Chem. Phys.* **5**, 1790–1805 (2003).
- ⁴⁵M. Akbar Ali and J. R. Barker, "Comparison of three isoelectronic multiple-well reaction systems: $\text{OH} + \text{CH}_2\text{O}$, $\text{OH} + \text{CH}_2\text{CH}_2$, and $\text{OH} + \text{CH}_2\text{NH}$," *J. Phys. Chem. A* **119**, 7578–7592 (2015).
- ⁴⁶Y. Zhao, B. Wang, H. Li, and L. Wang, "Theoretical studies on the reactions of formaldehyde with OH and OH^- ," *J. Mol. Struct.: THEOCHEM* **818**, 155–161 (2007).
- ⁴⁷G. de Souza Machado, E. M. Martins, L. Baptista, and G. F. Bauerfeldt, "Prediction of rate coefficients for the $\text{H}_2\text{CO} + \text{OH} \rightarrow \text{HCO} + \text{H}_2\text{O}$ reaction at combustion, atmospheric and interstellar medium conditions," *J. Phys. Chem. A* **124**, 2309–2317 (2020).
- ⁴⁸A. Aguado and M. Paniagua, "A new functional form to obtain analytical potentials of triatomic molecules," *J. Chem. Phys.* **96**, 1265 (1992).
- ⁴⁹B. J. Braams and J. M. Bowman, "Permutationally invariant potential energy surfaces in high dimensionality," *Int. Rev. Phys. Chem.* **28**, 577 (2009).
- ⁵⁰A. Aguado, C. Suárez, and M. Paniagua, "Accurate global fit of the H_4 potential energy surface," *J. Chem. Phys.* **101**, 4004 (1994).
- ⁵¹F. Murtagh, "Multilayer perceptrons for classification and regression," *Neurocomputing* **2**, 183–197 (1991).
- ⁵²D. C. Cireşan, U. Meier, J. Masci, L. M. Gambardella, and J. Schmidhuber, "Flexible, high performance convolutional neural networks for image classification," in *Twenty-Second International Joint Conference on Artificial Intelligence (AAAI, 2011)*.
- ⁵³D. K. Duvenaud, D. Maclaurin, J. Iparraguirre, R. Bombarell, T. Hirzel, A. Aspuru-Guzik, and R. P. Adams, "Convolutional networks on graphs for learning molecular fingerprints," *Adv. Neural Inf. Process. Syst.* **28**, 2224–2232 (2015).
- ⁵⁴S. A. King, "Minimal generating sets of non-modular invariant rings of finite groups," *J. Symbolic Comput.* **48**, 101–109 (2013).
- ⁵⁵W. Decker, G.-M. Greuel, G. Pfister, and H. Schönemann, *Singular 4-2-0—A Computer Algebra System for Polynomial Computations*, 2020; <http://www.singular.uni-kl.de>.
- ⁵⁶A. Paszke, S. Gross, F. Massa, A. Lerer, J. Bradbury, G. Chanan, T. Killeen, Z. Lin, N. Gimelshein, L. Antiga, A. Desmaison, A. Kopf, E. Yang, Z. DeVito, M. Raison, A. Tejani, S. Chilamkurthy, B. Steiner, L. Fang, J. Bai, and S. Chintala, "PyTorch: An imperative style, high-performance deep learning library," in *Advances in Neural Information Processing Systems 32*, edited by H. Wallach, H. Larochelle, A. Beygelzimer, F. d'Alché-Buc, E. Fox and R. Garnett (Curran Associates, Inc., 2019), pp. 8024–8035.
- ⁵⁷Y. Paukku, K. R. Yang, Z. Varga, and D. G. Truhlar, "Global *ab initio* ground-state potential energy surface of N_4 ," *J. Chem. Phys.* **139**, 044309 (2013).
- ⁵⁸Q. Yu and J. M. Bowman, "Ab initio potential for $\text{H}_3\text{O}^+ \rightarrow \text{H}^+ + \text{H}_2\text{O}$: A step to a many-body representation of the hydrated proton?," *J. Chem. Theory Comput.* **12**, 5284–5292 (2016).
- ⁵⁹J. Li, Z. Varga, D. G. Truhlar, and H. Guo, "Many-body permutationally invariant polynomial neural network potential energy surface for N_4 ," *J. Chem. Theory Comput.* **16**, 4822–4832 (2020).
- ⁶⁰A. Li and H. Guo, "A full-dimensional global potential energy surface of $\text{H}_3\text{O}^+(\tilde{a}^3\text{A})$ for the $\text{OH}^+(\tilde{X}^3\Sigma^-) + \text{H}_2(\tilde{X}^1\Sigma_g^+) \rightarrow \text{H}(\tilde{X}^2\Sigma) + \text{H}_2\text{O}^+(\tilde{X}^2\text{B}_1)$ reaction," *J. Phys. Chem. A* **118**, 11168–11176 (2014).
- ⁶¹A. Aguado, P. Barragán, R. Prosimiti, G. Delgado-Barrio, P. Villarreal, and O. Roncero, "A new accurate full dimensional potential energy surface of H_5^+ based on triatomics-in-molecule analytical functional form," *J. Chem. Phys.* **133**, 024306 (2010).
- ⁶²C. Sanz-Sanz, O. Roncero, M. Paniagua, and A. Aguado, "Full dimensional potential energy surface for the ground state of H_4^+ system based on triatomic-in-molecules formalism," *J. Chem. Phys.* **139**, 184302 (2013).
- ⁶³F. O. Ellison, "A method of diatomics in molecules. I. General theory and application to H_2O ," *J. Am. Chem. Soc.* **85**, 3540–3544 (1963).
- ⁶⁴F. O. Ellison, N. T. Huff, and J. C. Patel, "A method of diatomics in molecules. II. H and H_3^+ ," *J. Am. Chem. Soc.* **85**, 3544–3547 (1963).
- ⁶⁵A. Dorta-Urra, A. Zanchet, O. Roncero, and A. Aguado, "A comparative study of the $\text{Au} + \text{H}_2$, $\text{Au}^+ + \text{H}_2$, and $\text{Au}^- + \text{H}_2$ systems: Potential energy surfaces and dynamics of reactive collisions," *J. Chem. Phys.* **142**, 154301 (2015).
- ⁶⁶A. Zanchet, O. Roncero, and N. Bulut, "Quantum and quasi-classical calculations for the $\text{S}^+ + \text{H}_2(v, j) \rightarrow \text{SH}^+(v', j') + \text{H}$ reactive collisions," *Phys. Chem. Chem. Phys.* **18**, 11391–11400 (2016).
- ⁶⁷P. Ehrenfest, "XLVIII. Adiabatic invariants and the theory of quanta," *London, Edinburgh Dublin Philos. Mag. J. Sci.* **33**, 500–513 (1917).
- ⁶⁸T. Nagy and G. Lendvay, "Adiabatic switching extended to prepare semiclassically quantized rotational-vibrational initial states for quasiclassical trajectory calculations," *J. Phys. Chem. Lett.* **8**, 4621–4626 (2017).
- ⁶⁹M. Karplus, R. N. Porter, and R. D. Sharma, "Exchange reactions with activation energy. I. Simple barrier potential for (H, H_2) ," *J. Chem. Phys.* **43**, 3259–3287 (1965).
- ⁷⁰R. D. Levine and R. B. Bernstein, *Molecular Reaction Dynamics and Chemical Reactivity* (Oxford University Press, 1987).
- ⁷¹S. Wang, D. F. Davidson, and R. K. Hanson, "High temperature measurements for the rate constants of C1–C4 aldehydes with OH in a shock tube," *Proc. Combust. Inst.* **35**, 473–480 (2015).
- ⁷²R. A. Yetter, H. Rabitz, F. L. Dryer, R. G. Maki, and R. B. Klemm, "Evaluation of the rate constant for the reaction $\text{OH} + \text{H}_2\text{CO}$: Application of modeling and sensitivity analysis techniques for determination of the product branching ratio," *J. Chem. Phys.* **91**, 4088–4097 (1989).
- ⁷³I. R. Craig and D. E. Manolopoulos, "Quantum statistics and classical mechanics: Real time correlation functions from ring polymer molecular dynamics," *J. Chem. Phys.* **121**, 3368 (2004).
- ⁷⁴I. R. Craig and D. E. Manolopoulos, "Chemical reaction rates from ring polymer molecular dynamics," *J. Chem. Phys.* **122**, 084106 (2005).
- ⁷⁵I. R. Craig and D. E. Manolopoulos, "A refined ring polymer molecular dynamics theory of chemical reaction rates," *J. Chem. Phys.* **123**, 034102 (2005).
- ⁷⁶Y. V. Suleimanov, R. Colleparado-Guevara, and D. E. Manolopoulos, "Bimolecular reaction rates from ring polymer molecular dynamics: Application to $\text{H} + \text{CH}_4 \rightarrow \text{H}_2 + \text{CH}_3$," *J. Chem. Phys.* **134**, 044131 (2011).
- ⁷⁷Y. V. Suleimanov, F. J. Aoiz, and H. Guo, "Chemical reaction rate coefficients from ring polymer molecular dynamics: Theory and practical applications," *J. Phys. Chem. A* **120**, 8488 (2016).
- ⁷⁸R. Pérez de Tudela, F. J. Aoiz, Y. V. Suleimanov, and D. E. Manolopoulos, "Chemical reaction rates from ring polymer molecular dynamics: Zero point energy conservation in $\text{Mu} + \text{H}_2 \rightarrow \text{MuH} + \text{H}$," *J. Phys. Chem. Lett.* **3**, 493 (2012).
- ⁷⁹R. Pérez de Tudela, Y. V. Suleimanov, J. O. Richardson, V. Sáez Rábanos, W. H. Green, and F. J. Aoiz, "Stress test for quantum dynamics approximations: Deep tunneling in the muonium exchange reaction $\text{D} + \text{HMu} \rightarrow \text{DMu} + \text{H}$," *J. Phys. Chem. Lett.* **5**, 4219 (2014).
- ⁸⁰Y. V. Suleimanov, A. Aguado, S. Gómez-Carrasco, and O. Roncero, "Ring polymer molecular dynamics approach to study the transition between statistical and direct mechanisms in the $\text{H}_2 + \text{H}_3^+ \rightarrow \text{H}_3^+ + \text{H}_2$ reaction," *J. Phys. Chem. Lett.* **9**, 2133 (2018).
- ⁸¹Y. V. Suleimanov, J. W. Allen, and W. H. Green, "RPMDrate: Bimolecular chemical reaction rates from ring polymer molecular dynamics," *Comput. Phys. Commun.* **184**, 833–840 (2013).
- ⁸²H. C. Andersen, "Molecular dynamics simulations at constant pressure and/or temperature," *J. Chem. Phys.* **72**, 2384–2393 (1980).
- ⁸³A. Witt, S. D. Ivanov, M. Shiga, H. Forbert, and D. Marx, "On the applicability of centroid and ring polymer path integral molecular dynamics for vibrational spectroscopy," *J. Chem. Phys.* **130**, 194510 (2009).
- ⁸⁴M. Rossi, M. Ceriotti, and D. E. Manolopoulos, "How to remove the spurious resonances from ring polymer molecular dynamics," *J. Chem. Phys.* **140**, 234116 (2014).
- ⁸⁵S. Jang, A. V. Sinitskiy, and G. A. Voth, "Can the ring polymer molecular dynamics method be interpreted as real time quantum dynamics," *J. Chem. Phys.* **140**, 154103 (2014).
- ⁸⁶R. Korol, N. Bou-Rabee, and T. F. Miller III, "Cayley modifications for strongly stable path-integral and ring-polymer molecular dynamics," *J. Chem. Phys.* **151**, 124103 (2019).

⁸⁷N. Bulut, A. Aguado, C. Sanz-Sanz, and O. Roncero, "Quantum effects on the $D + H_3^+ \rightarrow H_2D^+ + H$ deuteration reaction and isotopic variants," *J. Phys. Chem. A* **123**, 8766 (2019).

⁸⁸R. A. Marcus, "Lifetimes of active molecules. I," *J. Chem. Phys.* **20**, 352–354 (1952).

⁸⁹R. A. Marcus, "Lifetimes of active molecules. II," *J. Chem. Phys.* **20**, 355–359 (1952).

⁹⁰J. O. Richardson and S. C. Althorpe, "Ring-polymer molecular dynamics rate-theory in the deep-tunneling regime: Connection with semiclassical instanton theory," *J. Chem. Phys.* **131**, 214106 (2009).